This is the accepted manuscript made available via CHORUS. The article has been published as:

Electronic nematic order in the normal state of strontium ruthenate

Ryan S. Russell, Hari P. Nair, Kyle M. Shen, Darrell G. Schlom, and John W. Harter

Phys. Rev. B **108**, L081105 — Published 9 August 2023

DOI: 10.1103/PhysRevB.108.L081105

Electronic nematic order in the normal state of strontium ruthenate

Ryan Russell,[1] Hari P. Nair,[2] Kyle M. Shen,[3,4] Darrell G. Schlom,[2,4,5] and John W. Harter[1,*]

[1] *Materials Department, University of California, Santa Barbara, California 93106, USA*
[2] *Department of Materials Science and Engineering, Cornell University, Ithaca, New York 14853, USA*
[3] *Physics Department, Cornell University, Ithaca, New York 14853, USA*
[4] *Kavli Institute at Cornell for Nanoscale Science, Ithaca, New York 14853, USA*
[5] *Leibniz-Institut für Kristallzüchtung, 12489 Berlin, Germany*

(Dated: July 20, 2023)

Despite significant achievements in characterizing the properties of Sr_2RuO_4 over the last three decades, the precise nature of its electronic ground state is still unresolved. In this work, we provide a missing piece of the puzzle by uncovering evidence of electronic nematic order in the normal state of Sr_2RuO_4, revealed by ultrafast time-resolved optical dichroism measurements of uniaxially strained thin films. This nematic order, whose domains are aligned by the strain, spontaneously breaks the four-fold rotational symmetry of the crystal. The temperature dependence of the dichroism resembles an Ising-like order parameter, and optical pumping induces a coherent oscillation of its amplitude mode. The existence of electronic nematic order in the normal state of Sr_2RuO_4 may have consequences for the form and mechanism of superconductivity in this material.

I. INTRODUCTION

The study of Sr_2RuO_4 entered a new era after the recent observation of a reduction in the Knight shift at the onset of superconductivity [1], which overturned the long-favored chiral p-wave triplet pairing scenario. Researchers are presently faced with an array of sometimes contradictory results, and it is clear that a fundamental piece of the Sr_2RuO_4 puzzle is still missing [2]. It has long been believed that the normal state of Sr_2RuO_4 is a conventional quasi-two-dimensional Fermi liquid with moderate correlations [2, 3]. Evidence of any deviation from conventional Fermi liquid behavior would have significant consequences for theoretical proposals and the interpretation of experiments. In this work, we present such evidence. Motivated by recent transverse resistivity experiments [4], we use optical dichroism measurements of high-quality epitaxially strained thin films to uncover evidence of electronic nematic order in the normal state of Sr_2RuO_4.

Nematic order spontaneously breaks rotational symmetry while preserving translational symmetry. In a tetragonal crystal, nematicity results in a lowering of symmetry to an orthorhombic unit cell where the a and b directions become nonequivalent. The spontaneous nature of the symmetry breaking invariably leads to the formation of domains related by 90° rotations, whose average over long length scales retains the parent tetragonal symmetry. Thus, directly detecting nematic symmetry breaking with macroscopic probes generally requires stabilizing the formation of one type of domain, akin to structural detwinning. Uniaxial strain is an ideal external conjugate field by which one can achieve this effect. In the iron-based superconductors, for example, uniaxial strain has been used to study nematic order with optical, transport, and photoemission experiments [5–9]. Here, we take advantage of uniaxial epitaxial strain to enable macroscopic transient optical reflectivity measurements of electronic nematic order in Sr_2RuO_4.

We study high-quality thin films of (001)-oriented Sr_2RuO_4 grown by molecular-beam epitaxy, as described in Ref. 10. The films are 30 nm thick and coherently strained to (110) $NdGaO_3$ single-crystal substrates [11], guaranteeing a clean, uniform strain field over the entire sample area. Transport measurements confirm the films are superconducting, with a critical temperature of $T_c \approx 1.4$ K (Supplemental Materials [12]). $NdGaO_3$ induces a small uniaxial (B_{1g}) strain of $a/b - 1 \approx 0.3\%$ at low temperatures, where a and b are the in-plane lattice constants of the Sr_2RuO_4 film. Specifically, a and b correspond to the $[1\bar{1}0]$ and [001] spacings, respectively, of the (110) $NdGaO_3$ substrate in the $Pbnm$ setting [11] [Fig. 1(a)]. Strain has been used extensively in recent years to study the Lifshitz transition in Sr_2RuO_4 and to enhance superconductivity [13–19]. We emphasize, however, that the magnitude of uniaxial strain that we employ is not sufficient to induce a Lifshitz transition (estimated in Ref. 19 to be $\varepsilon_{xx} - \varepsilon_{yy} \approx 0.7\%$), and moreover the epitaxial strain is biaxially compressive (-0.1% in the a direction and -0.4% in the b direction at low temperatures) relative to bulk Sr_2RuO_4 [20, 21], which is known to move the Fermi level *away* from the van Hove singularity rather than towards it [14]. Thus, the effects that we measure are due to a relatively weak uniaxial perturbation of the electronic structure and are not expected to be driven by density of states enhancements or changes in band topology.

* Corresponding author: harter@ucsb.edu

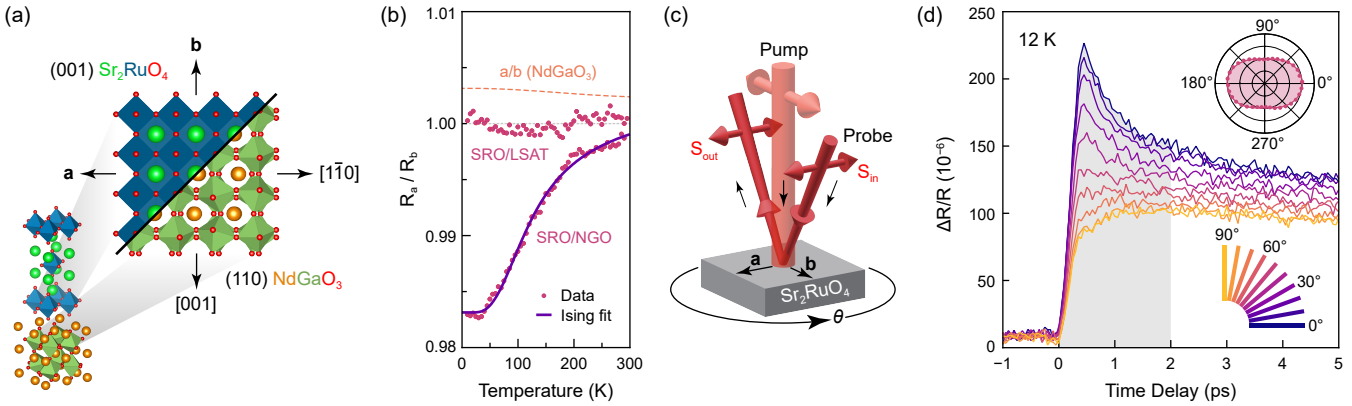


FIG. 1. Static and transient optical measurements. (a) Crystallographic directions in the film and substrate. For (001) Sr_2RuO_4 on (110) $NdGaO_3$, the a-axis corresponds to [1$\bar{1}$0] $NdGaO_3$ and the b-axis corresponds to [001] $NdGaO_3$. (b) Reflectivity anisotropy R_a/R_b versus temperature for films grown on $NdGaO_3$ (SRO/NGO) and LSAT (SRO/LSAT). A fit to an Ising model of nematic order is shown, as well as the lattice constant ratio a/b for films strained to $NdGaO_3$ (from Ref. 11). (c) Illustration of the pump-probe experimental geometry. The pump and probe beams remain fixed in a cross-polarized configuration while the sample is rotated about its surface normal. $\theta = 0°$ when the probe is polarized along the a-axis (as shown) and $\theta = 90°$ when polarized along the b-axis. (d) Raw transient reflectivity curves for several values of θ at 12 K. A clear anisotropy is observed in the picosecond-scale transient response. The inset shows a polar plot of $\Delta R/R$ integrated from 0 to 2 ps (gray shaded region).

II. EXPERIMENTAL RESULTS

We first examine the static reflectivity anisotropy, defined as the ratio of reflectivity for light polarized along the a-axis to that along the b-axis. Figure 1(b) shows the measured anisotropy versus temperature using a probe wavelength of 800 nm, where a striking dichroism is apparent. We find a decrease in reflectivity along the (long) a-axis relative to the (short) b-axis, which becomes more pronounced at lower temperatures. At the lowest temperatures, the maximum reflectivity anisotropy is 1.7%, more than five times larger than the uniaxial strain imposed by the substrate (0.3%). Similar behavior has been observed in detwinned FeSe, where the reflectivity anisotropy was taken as a proxy for the nematic order parameter [9]. To eliminate the possibility that the dichroism is merely due to structural orthorhombicity, we include in the figure the temperature-dependent lattice constant ratio a/b for films strained to $NdGaO_3$. If the anisotropy is due to simple $a \neq b$ structural effects, we would expect a linear proportionality with the substrate orthorhombicity (Supplemental Materials [12]). Instead, we observe the dichroism grow by an order of magnitude upon cooling, while the substrate orthorhombicity only increases by 30%. As a control, we also measure the reflectivity of Sr_2RuO_4 grown on (001) $(LaAlO_3)_{0.29}(SrTa_{1/2}Al_{1/2}O_3)_{0.71}$ (LSAT), which is tetragonal and induces no uniaxial strain ($a = b$) [22]. In this case, we detect no appreciable dichroism. Our static optical anisotropy measurements suggest that the electronic structure of Sr_2RuO_4 possesses either spontaneous nematic order (scenario I) or a large nematic susceptibility (scenario II). In scenario I, an electronic instability results in the formation of microscopic nematic domains, with one orientation favored by the uniaxial strain over the other. This imbalance induces a net macroscopic anisotropy in the optical response. In scenario II, the weak uniaxial strain drives a strong electronic nematic response via a large nematic susceptibility. Without the strain, however, the electronic structure would retain tetragonal symmetry at all temperatures. Both scenarios are consistent with an absence of dichroism in films grown on LSAT.

Now that signatures of electronic nematic order in the optical dichroism have been established, we next turn to measuring the ultrafast response of the order. As we will show, this reveals much larger signatures of nematicity than the static reflectivity and enables the extraction of dynamical information. We use a standard pump-probe transient reflectivity technique to measure changes in the dichroism induced by an ultrafast (∼50 fs) pump pulse of wavelength 760 nm and fluence ∼25 $\mu J/cm^2$. To eliminate any possible anisotropy due to the polarization of the pump, we keep the pump and probe pulses fixed in a cross-polarized configuration and rotate the sample about its surface normal [Fig. 1(c)]. Like the static reflectivity, we uncover a pronounced anisotropy of the transient response. Figure 1(d) shows raw transients of the relative change in reflectivity $\Delta R/R$ versus pump-probe time delay at 12 K for several angles between the a-axis (0°) and the b-axis (90°). A clear breaking of tetragonal symmetry is apparent: for optical polarization parallel to the a-axis, we observe a sharp peak in $\Delta R/R$ that decays over a ∼1 ps timescale, whereas for polarization parallel to the b-axis, we observe only a flat step. This nematic ($C_4 \rightarrow C_2$) symmetry breaking can be seen more clearly in a polar plot of the area under the curve (inset). While

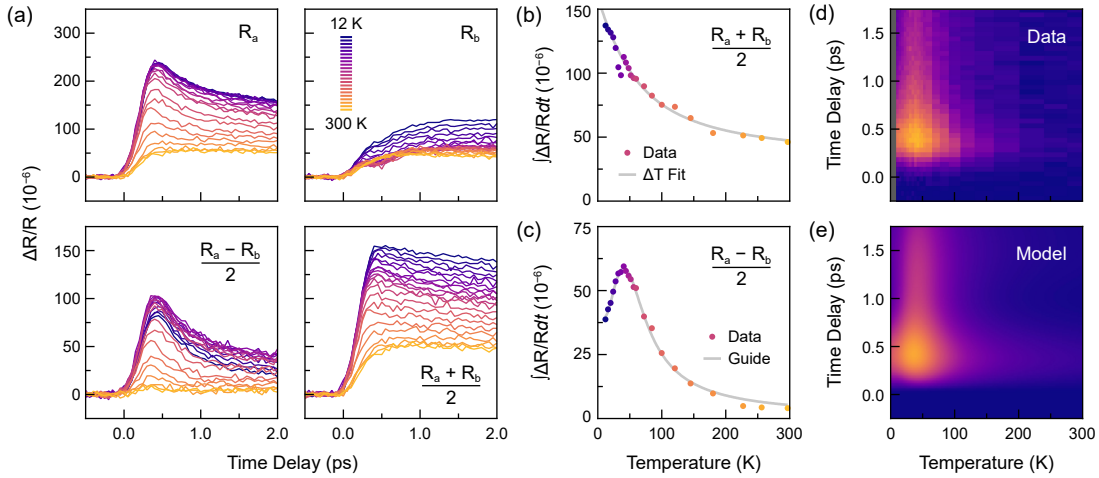


FIG. 2. Temperature dependence of transient reflectivity. (a) $\Delta R/R$ for selected temperatures between 12 K and 300 K for polarization along the a-axis (upper left), b-axis (upper right), their difference (lower left), and their sum (lower right). (b) Temperature dependence of the average value of $\Delta(R_a + R_b)/2R$ between 1.5 and 2 ps, representing the isotropic component of the transient response. The response monotonically decreases with increasing temperature. The gray line is a fit to the sample temperature change. (c) Temperature dependence of the average value of $\Delta(R_a - R_b)/2R$ between 0 and 2 ps, representing the nematic component of the transient response. An unusual non-monotonic behavior is observed. (d) Two-dimensional joint time delay and temperature dependence of $\Delta(R_a - R_b)/2R$. (e) Corresponding depiction generated by fitting to the Ising nematic model.

the static reflectivity shows a modest 1.7% anisotropy, the transient reflectivity anisotropy exceeds 100%. Ultrafast optical anisotropies of this magnitude are routinely observed in the nematic phase of iron-based superconductors [23–27]. Sr_2RuO_4 is a multiband system with strong hybridization between the three Ru t_{2g} orbitals and six O $p_{x,y}$ orbitals, and photon absorption at our pump energy (1.6 eV) results from a mixture of intraband and interband electronic transitions [28]. Strongest absorption is expected between occupied $d_{xz,yz}$ states (forming the α and β bands) and unoccupied $d_{x^2-y^2}$ states. These directly photoexcited "hot" electrons will subsequently thermalize with the d_{xy} electrons forming the γ band, which contain the electronic states with most relevance to nematic order (see the microscopic model discussed below). Our experiments are carried out in the low excitation density limit, and the conventional expectation that electron-phonon thermalization is slower than electron-electron thermalization does not necessarily hold [29]. More specifically, hot phonons may be generated through rapid thermalization with the hot electrons, followed by a slower thermalization with the rest of the system, as has been observed in time-resolved studies of the cuprates [30]. As we discuss in more detail below, we see evidence of this slower electron-electron thermalization in the thermal response of the nematic degrees of freedom.

Figure 2(a) shows measurements at several temperatures between 12 K and 300 K for polarization along the a-axis (R_a) and b-axis (R_b). To isolate temperature-dependent changes in the anisotropy from other effects, we also show the difference ($R_a - R_b$) and sum ($R_a + R_b$). We see that the sharp peak in $\Delta R/R$ is entirely due to the nematicity of the material, while the flat step after time-zero represents the isotropic component of the optical response. Moreover, while the isotropic response monotonically decreases with increasing temperature [Fig. 2(b)], we uncover an unusual non-monotonic temperature dependence of the nematic component of the response [Fig. 2(c)]. The isotropic transient response is likely caused by an increase in temperature ΔT after absorption of the pump. Assuming each pump pulse deposits a fixed energy ΔE into the electronic subsystem (heat capacity $C = \gamma T$), it follows that $\Delta T_{\max}(T) = \sqrt{T^2 + (2\Delta E/\gamma)} - T$. Using the value of γ from Ref. 31 and ΔE calculated from our fluence, we find $(2\Delta E/\gamma) \approx (80\ \mathrm{K})^2$ (Supplemental Materials [12]). A function of the form $g(T) = \alpha + \beta\Delta T_{\max}(T)$ fits the isotropic component extremely well [gray line in Fig. 2(b)]. We use this fact to scale the data at each temperature to match $g(T)$ and correct for laser fluctuations during the experiment, where, for example, the two data points near ∼35 K are otherwise anomalously low. This normalization procedure is used for the remainder of our analysis.

III. ISING NEMATIC MODEL OF DATA

A saturation at low temperatures is evident in the static dichroism [Fig. 1(b)], resembling an Ising-like order parameter. To quantitatively analyze the data, we therefore develop a heuristic mean-field Ising model of the nematic order, which can describe both scenarios discussed above. Within the model, we define an order parame-

ter ϕ that takes the values $+1$ or -1, corresponding to a nematic director oriented along the a- or b-axis, respectively. The Hamiltonian is

$$\mathcal{H} = -\frac{1}{2}\sum_{i,j} U(\mathbf{r}_i - \mathbf{r}_j)\phi_i\phi_j - F\sum_i \phi_i,$$

where i and j label unit cells, $U(\mathbf{r})$ is the interaction energy (related to the stiffness of the nematic order), and F is the uniaxial strain field, which favors $+1$ domains over -1 domains. Within mean-field theory, the average order parameter $\langle\phi\rangle$ satisfies the self-consistency equation

$$\langle\phi\rangle = \tanh\left(\frac{U\langle\phi\rangle + F}{k_B T}\right),$$

where $U = \sum_i U(\mathbf{r}_i)/2 = k_B T_c$ defines the critical temperature of the nematic phase transition. We assume the measured optical anisotropy is proportional to the order parameter ($R_a/R_b - 1 \propto \langle\phi\rangle$) and fit the data to this functional form. The least-squares fit, included in Fig. 1(b), yields the parameters $U = 53 \pm 8$ K and $F = 53 \pm 7$ K. Excellent agreement with the data is achieved despite the relative simplicity of our model. Taking it at face value, the model predicts a critical temperature of $T_c \approx 50$ K, where global nematic order spontaneously condenses following scenario I. In reality, this transition is spread over a wide temperature range due to the large magnitude of the symmetry-breaking uniaxial strain field. Scenario II, where nematic order does not occur without strain, would require $U \leq 0$, which is not consistent with our data. Based on the success of this simple Ising nematic model, we will continue to use it to quantitatively analyze the data.

Figure 1(b) shows that the onset of nematic order reduces the optical reflectivity along the a-axis. After the pump pulse, this reflectivity increases. It follows that the effect of the pump is to suppress the nematic order, likely through a transient increase in temperature. To model this, we assume the dichroism is proportional to the nematic order parameter ϕ. The measured change in dichroism is therefore proportional to the change in ϕ:

$$\Delta(R_a - R_b)/R \propto (1+\delta)\phi(T + \Delta T) - \phi(T),$$

where $\phi(T)$ is the equilibrium value of the order parameter at the measurement temperature T, ΔT is the increase in electronic temperature after absorption of the pump energy, and $\delta < 0$ represents a non-thermal suppression of the order parameter amplitude by the pump pulse. The previously developed Ising model provides an expression for $\phi(T)$. The temperature increase ΔT is not necessarily instantaneous. Instead, we allow the temperature of the electrons to rise to some time-dependent fraction $0 \leq f(t) \leq 1$ of $\Delta T_{\max}$ [$\Delta T(t) = f(t)\Delta T_{\max}$]. With this model, we fit the transient optical data at all time delays and all temperatures simultaneously. The fit includes three global parameters (U, F, and a fixed scaling factor) and two time-dependent parameters [$\delta(t)$ and $f(t)$]. The results of the fit, shown in Fig. 3(a), are excellent ($R^2 = 0.994$).

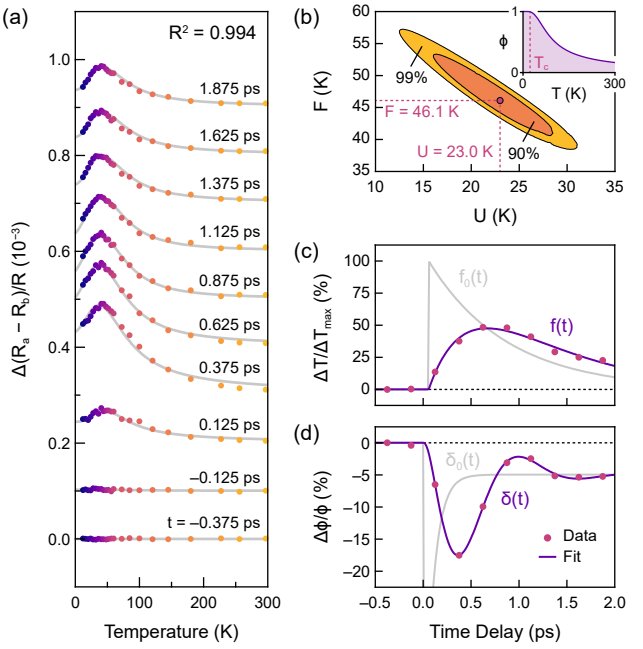


FIG. 3. Ising model fit of optical anisotropy. (a) $\Delta(R_a - R_b)/R$ versus temperature for selected time delays after the pump pulse. Curves are offset by 10^{-4}. Gray lines show the global fit to the Ising nematic model, as described in the text. (b) Confidence regions for the Ising parameters U and F computed through an F-test. $U > 0$ with greater than 99% confidence, implying the existence of spontaneous nematic order. The inset shows the order parameter $\phi(T)$ together with the critical temperature T_c for spontaneous nematic order when $F = 0$. (c) Electronic temperature increase versus time delay as a fraction of the calculated maximum increase. Also shown is a fit to the solution of the heat equation $df/dt = k(f_0 - f)$ (purple curve) with background electronic temperature f_0 (gray curve). (d) Relative suppression of the nematic order versus time delay, showing a coherent oscillation of the order parameter amplitude. Also shown is a fit to a damped harmonic oscillator (purple curve) with a pump-induced displacement of the equilibrium amplitude (gray curve).

A number of salient points are uncovered by the fit: **(1)** The non-monotonic temperature dependence of the dichroism [Fig. 2(c)] is a result of the flattening of the nematic order parameter at low temperatures ($d\phi/dT \to 0$ as $T \to 0$), which reduces the effect of pump heating. At the lowest temperatures, the pump-induced change in temperature ΔT does not induce a large change in the order parameter $\Delta\phi$, so the measured $\Delta(R_a - R_b)/R$ correspondingly drops. **(2)** Uncertainties in the fit parameters U and F are correlated, which is a result of their coupled influence on $\phi(T)$. The F-test-derived confidence regions displayed in Fig. 3(c), however, show that $U > 0$ with high confidence. Crucially, if the uniaxial strain were to be removed ($F \to 0$), spontaneous nematic order would still occur within the model at $T_c = U$. Within the ap-

plicability of the model, this implies that the nematic order we observe is spontaneous (scenario I). We note that a more realistic model, such as one that includes a temperature-dependent proportionality constant or a nonlinear dependence on the conjugate strain field, may alter this interpretation. **(3)** While we extract a value for F similar to that of the static measurement (46 K versus 53 K), the value of U is smaller (23 K versus 53 K). We conjecture that repeatedly exciting the sample with high-fluence optical pulses does not allow it to completely return to equilibrium, causing a net suppression of the order parameter. This subsequently renormalizes the average interaction energy U. **(4)** Figure 3(c) shows that the nematic electron temperature rises to ∼50% of the maximum calculated increase $\Delta T_{\max}$ within ∼0.6 ps. This is consistent with a scenario where the pump energy is first absorbed by background "hot" electrons during the pulse (∼50 fs) and then transferred at a slower timescale to the nematic degrees of freedom via thermal equilibration mediated by electron-electron interactions. To make this picture more quantitative, we fit $f(t)$ to the heat equation $df/dt = k(f_0 - f)$ (Supplemental Materials [12]), where $f_0(t) = e^{-t/\tau}$ represents the temperature of the hot electron (and potentially hot phonon [30]) background, with timescale τ for equilibration with the rest of the system. We find excellent agreement with the data for $\tau = 0.82$ ps and $k^{-1} = 0.47$ ps. The latter parameter represents a relatively slow thermalization between the hot particles and the nematic order. This slow thermalization is expected in the low excitation density limit due to a reduced phase space for electron-electron scattering by Pauli blocking [29]. **(5)** The non-thermal suppression of the order parameter after the pump pulse [Fig. 3(d)] reveals a coherent oscillation, which can be understood with a damped harmonic oscillator model: $d^2\delta/dt^2 + 2\gamma d\delta/dt + \omega_0^2(\delta - \delta_0) = 0$, where γ is the damping rate, ω_0 is the natural frequency, and δ_0 is the pump-induced displacement of the order parameter amplitude. A solution to this equation fits the data well if $\delta_0(t) = \alpha e^{-t/\tau} + \beta$, representing a sharp impulsive suppression at $t = 0$ followed by a rapid recovery ($\tau = 0.09$ ps) to a displaced equilibrium amplitude $\beta = -5.0\%$ relative to the initial value [gray curve in Fig. 3(d)]. We extract a frequency $\omega_0/2\pi = 0.89$ THz for the nematic amplitude mode.

IV. MICROSCOPIC MODEL

The foregoing optical experiments suggest that Sr_2RuO_4 supports a high-temperature Ising-like nematic order parameter with an order-disorder phase transition below ∼50 K. To put forth a possible microscopic origin for this order, we turn to the Emery model, first used to describe hole doping of CuO_2 planes in cuprate superconductors away from half filling [32]. Here, we use the model to study intra-unit-cell nematic order in RuO_2 planes with fillings adjacent to the van Hove singularity

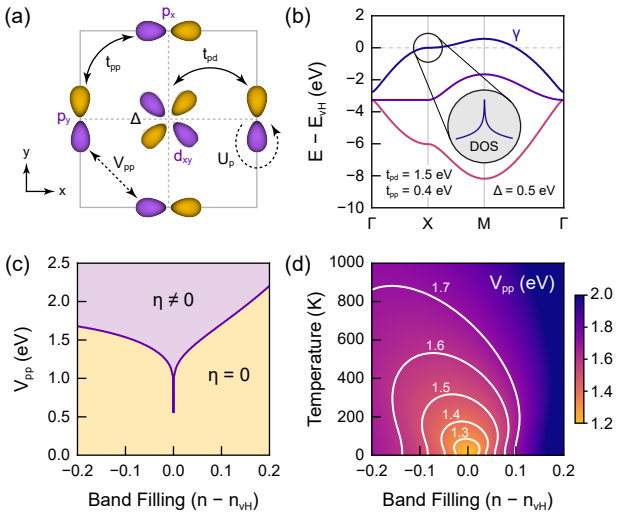


FIG. 4. Microscopic model of nematic order in Sr_2RuO_4. (a) Unit cell of the RuO_2 plane showing the three-orbital basis (Ru d_{xy} and O p_x and p_y) of the Emery model. Hopping integrals (solid lines) and interaction parameters (dashed lines) are defined following Ref. 34. (b) Resulting tight-binding band structure, with parameters taken from Ref. 35. (c) Interaction–filling phase diagram showing the critical value of V_{pp} necessary to produce a nematic ground state ($\eta \neq 0$). (d) Temperature–filling phase diagram for different values of V_{pp}. Panels (c) and (d) were calculated for $U_p = 4.4$ eV [35].

of the γ band [33]. Our mean-field analysis closely follows Ref. 34 (Supplemental Materials [12]). Figure 4(a) shows the hopping and interaction parameters defined within the model, and Fig. 4(b) shows the resulting band structure. Of central importance are the Coulomb repulsion between neighboring oxygen p-orbitals (V_{pp}), which favors a nematic charge order $\eta = n_x^p - n_y^p$ with different electron densities on the p_x and p_y orbitals, and the van Hove singularity of the γ band at the X point, which leads to a diverging density of states that supports electronic instabilities by reducing the energy cost to redistribute orbital density. Figure 4(c) shows the mean-field ground state phase diagram as a function of V_{pp} and filling. A nematic phase is stabilized for sufficiently large values of V_{pp} that depend on the proximity to the van Hove filling. Bulk Sr_2RuO_4 has $n - n_{\mathrm{vH}} \approx -0.2$ [33], which requires an interaction strength $V_{pp} > 1.7$ eV to stabilize nematic order. The full temperature–filling phase diagram is displayed in Fig. 4(d), where it is seen that such order, if it exists, condenses well above room temperature. The model shows that Sr_2RuO_4 is exceptionally close to a nematic instability, and offers a plausible microscopic picture of an Ising-like ($\eta = \pm\eta_0$) nematic charge order. We conjecture that at high temperatures this nematicity is spatially disordered at the nanoscale, but shows an order-disorder phase transition to a globally nematic state at lower temperatures.

V. CONCLUSION

In conclusion, optical dichroism measurements of epitaxially strained thin films strongly support the existence of electronic nematic order in Sr_2RuO_4. By fitting our data to a simple Ising model, we conjecture that this order emerges spontaneously at low temperatures through an order-disorder transition, rather than through a large nematic susceptibility. Outside the framework of this model, however, the possibility remains that the nematic order we observe originates through a large but finite nematic susceptibility. Our results corroborate the angle-resolved transverse resistivity measurements that first uncovered electronic nematicity in Sr_2RuO_4 [4]. While electrical transport and optical reflectivity are disparate probes operating at different energy scales, they both show clear signatures of two-fold electronic anisotropy. Furthermore, although transport can be sensitive to non-local effects such as defect scattering, especially in a material with ostensible microscopic nematic domains, optical reflectivity is a local, bulk-sensitive probe. Our findings also offer a new perspective on the Fermi liquid crossover at $T_{\mathrm{FL}} \sim 40$ K observed by Hall transport [36–38], optical spectroscopy [28], and nuclear magnetic resonance [39, 40]. We speculate that the crossover is directly related to nematicity, which appears to develop at the same temperature. Indeed, such a Fermi liquid crossover has been theoretically shown to emerge in the vicinity of an Ising nematic quantum critical point [41–43]. Nematic order also offers a natural explanation for the checkerboard charge order observed at the surface of Sr_2RuO_4 by scanning tunneling microscopy [44]. Rather than surface nematic order emerging as a secondary effect, we find it likely that the checkerboard charge order is the secondary response, emerging from a combination of bulk nematicity and surface octahedral rotations. An important open question is to what extent electronic nematic order in the normal state of Sr_2RuO_4 influences the likelihood of different forms of superconductivity at lower temperatures. Future experimental and theoretical work is necessary to address this principal question.

ACKNOWLEDGMENTS

We thank Dr. Ludi Miao for performing electrical resistivity measurements. This work was primarily supported by the U.S. Department of Energy, Office of Basic Energy Sciences under Award No. DE-SC0019414. Thin film synthesis was funded in part by the Gordon and Betty Moore Foundation's EPiQS Initiative through Grant Nos. GBMF3850 and GBMF9073 to Cornell University. Substrate preparation was, in part, facilitated by the Cornell NanoScale Facility, a member of the National Nanotechnology Coordinated Infrastructure (NNCI), which is supported by the National Science Foundation (Grant No. NNCI-2025233). Additional support was provided by AFOSR FA9550-21-1-0168.

[1] A. Pustogow, Y. Luo, A. Chronister, Y.-S. Su, D. A. Sokolov, F. Jerzembeck, A. P. Mackenzie, C. W. Hicks, N. Kikugawa, S. Raghu, E. D. Bauer, S. E. Brown. Constraints on the superconducting order parameter in Sr_2RuO_4 from oxygen-17 nuclear magnetic resonance. *Nature* **574**, 72 (2019).

[2] A. P. Mackenzie, T. Scaffidi, C. W. Hicks, Y. Maeno. Even odder after twenty-three years: the superconducting order parameter puzzle of Sr_2RuO_4. *npj Quantum Mater.* **2**, 40 (2017).

[3] A. P. Mackenzie, Y. Maeno. The superconductivity of Sr_2RuO_4 and the physics of spin-triplet pairing. *Rev. Mod. Phys.* **75**, 657 (2003).

[4] J. Wu, H. P. Nair, A. T. Bollinger, X. He, I. Robinson, N. J. Schreiber, K. M. Shen, D. G. Schlom, I. Božović. Electronic nematicity in Sr_2RuO_4. *Proc. Natl. Acad. Sci.* **117**, 10654 (2020).

[5] A. Dusza, A. Lucarelli, F. Pfuner, J.-H. Chu, I. R. Fisher, L. Degiorgi. Anisotropic charge dynamics in detwinned $Ba(Fe_{1-x}Co_x)_2As_{1-x}$. *EPL* **93**, 37002 (2011).

[6] M. A. Tanatar, E. C. Blomberg, A. Kreyssig, M. G. Kim, N. Ni, A. Thaler, S. L. Bud'ko, P. C. Canfield, A. I. Goldman, I. I. Mazin, R. Prozorov. Uniaxial-strain mechanical detwinning of $CaFe_2As_2$ and $BaFe_2As_2$ crystals: Optical and transport study. *Phys. Rev. B* **81**, 184508 (2010).

[7] J.-H. Chu, J. G. Analytis, K. De Greve, P. L. McMahon, Z. Islam, Y. Yamamoto, I. R. Fisher. In-Plane Resistivity Anisotropy in an Underdoped Iron Arsenide Superconductor. *Science* **329**, 824 (2010).

[8] M. Yi, D. Lu, J.-H. Chu, J. G. Analytis, A. P. Sorini, A. F. Kemper, B. Moritz, S.-K. Mo, R. G. Moore, M. Hashimoto, W.-S. Lee, Z. Hussain, T. D. Devereaux, I. R. Fisher, Z.-X. Shen. Symmetry-breaking orbital anisotropy observed for detwinned $Ba(Fe_{1-x}Co_x)_2As_2$ above the spin density wave transition. *Proc. Natl. Acad. Sci.* **108**, 6878 (2011).

[9] M. Chinotti, A. Pal, L. Degiorgi, A. E. Böhmer, P. C. Canfield. Optical anisotropy in the electronic nematic phase of FeSe. *Phys. Rev. B* **96**, 121112(R) (2017).

[10] H. P. Nair, J. P. Ruf, N. J. Schreiber, L. Miao, M. L. Grandon, D. J. Baek, B. H. Goodge, J. P. C. Ruff, L. F. Kourkoutis, K. M. Shen, D. G. Schlom. Demystifying the growth of superconducting Sr_2RuO_4 thin films. *APL Mater.* **6**, 101108 (2018).

[11] D. Savytskii, L. Vasylechko, A. Senyshyn, A. Matkovskii, C. Bähtz, M. L. Sanjuán, U. Bismayer, M. Berkowski. Low-temperature structural and Raman studies on rare-earth gallates. *Phys. Rev. B* **68**, 024101 (2003).

[12] See Supplemental Material at [URL will be inserted by publisher] for experimental methods, nematicity across several relaxation timescales, measurements of film on an LSAT substrate, calculation of pump-induced temperature change, derivation of heat equation, and microscopic model of nematic charge order.

[13] C. W. Hicks, D. O. Brodsky, E. A. Yelland, A. S. Gibbs, J. A. N. Bruin, M. E. Barber, S. D. Edkins, K. Nishimura, S. Yonezawa, Y. Maeno, A. P. Mackenzie. Strong Increase of T_c of Sr_2RuO_4 Under Both Tensile and Compressive Strain. *Science* **344**, 283 (2014).

[14] B. Burganov, C. Adamo, A. Mulder, M. Uchida, P. D. C. King, J. W. Harter, D. E. Shai, A. S. Gibbs, A. P. Mackenzie, R. Uecker, M. Bruetzam, M. R. Beasley, C. J. Fennie, D. G. Schlom, K. M. Shen. Strain Control of Fermiology and Many-Body Interactions in Two-Dimensional Ruthenates. *Phys. Rev. Lett.* **116**, 197003 (2016).

[15] A. Steppke, L. Zhao, M. E. Barber, T. Scaffidi, F. Jerzembeck, H. Rosner, A. S. Gibbs, Y. Maeno, S. H. Simon, A. P. Mackenzie, C. W. Hicks. Strong peak in T_c of Sr_2RuO_4 under uniaxial pressure. *Science* **355**, 148 (2017).

[16] V. Sunko, E. A. Morales, I. Marković, M. E. Barber, D. Milosavljević, F. Mazzola, D. A. Sokolov, N. Kikugawa, C. Cacho, P. Dudin, H. Rosner, C. W. Hicks, P. D. C. King, A. P. Mackenzie. Direct observation of a uniaxial stress-driven Lifshitz transition in Sr_2RuO_4. *npj Quantum Mater.* **4**, 46 (2019).

[17] V. Grinenko, S. Ghosh, R. Sarkar, J.-C. Orain, A. Nikitin, M. Elender, D. Das, Z. Guguchia, F. Brückner, M. E. Barber, J. Park, N. Kikugawa, D. A. Sokolov, J. S. Bobowski, T. Miyosho, Y. Maeno, A. P. Mackenzie, H. Luetkens, C. W. Hicks, H.-H. Klauss. Split superconducting and time-reversal symmetry-breaking transitions in Sr_2RuO_4 under stress. *Nat. Phys.* **17**, 748 (2021).

[18] Y.-S. Li, N. Kikugawa, D. A. Sokolov, F. Jerzembeck, A. S. Gibbs, Y. Maeno, C. W. Hicks, J. Schmalian, M. Nicklas, A. P. Mackenzie. High-sensitivity heat-capacity measurements on Sr_2RuO_4 under uniaxial pressure. *Proc. Natl. Acad. Sci.* **118**, e2020492118 (2021).

[19] M. E. Barber, F. Lechermann, S. V. Streltsov, S. L. Skornyakov, S. Ghosh, B. J. Ramshaw, N. Kikugawa, D. A. Sokolov, A. P. Mackenzie, C. W. Hicks, I. I. Mazin. Role of correlations in determining the Van Hove strain in Sr_2RuO_4. *Phys. Rev. B* **100**, 245139 (2019).

[20] T. Vogt, D. J. Buttrey. Low-temperature structural behavior of Sr_2RuO_4. *Phys. Rev. B* **52**, R9843 (1995).

[21] O. Chmaissem, J. D. Jorgensen, H. Shaked, S. Ikeda, Y. Maeno. Thermal expansion and compressibility of Sr_2RuO_4. *Phys. Rev. B* **57**, 5067 (1998).

[22] M. Steins, J. Doerschel, P. Reiche. Crystal structure of aluminium lanthanum strontium tantalum oxide, $(La_{0.272}Sr_{0.728})(Al_{0.648}Ta_{0.352})O_3$. *Zeitschrift für Kristallographie - New Crystal Structures* **212**, 77 (1997).

[23] L. Stojchevska, T. Mertelj, J.-H. Chu, I. R. Fisher, D. Mihailovic. Doping dependence of femtosecond quasiparticle relaxation dynamics in $Ba(Fe,Co)_2As_2$ single crystals: Evidence for normal-state nematic fluctuations. *Phys. Rev. B* **86**, 024519 (2012).

[24] C.-W. Luo, P. C. Cheng, S.-H. Wang, J.-C. Chiang, J.-Y. Lin, K.-H. Wu, J.-Y. Juang, D. A. Chareev, O. S. Volkova, A. N. Vasiliev. Unveiling the hidden nematicity and spin subsystem in FeSe. *npj Quantum Mater.* **2**, 32 (2017).

[25] S. Liu, C. Zhang, Q. Deng, H. Wen, J. Li, E. E. M. Chia, X. Wang, M. Xiao. Transient electronic anisotropy in overdoped $NaFe_{1-x}Co_xAs$ superconductors. *Phys. Rev. B* **97**, 020505(R) (2018).

[26] E. Thewalt, I. M. Hayes, J. P. Hinton, A. Little, S. Patankar, L. Wu, T. Helm, C. V. Stan, B. Tamura, J. G. Analytis, J. Orenstein. Imaging Anomalous Nematic Order and Strain in Optimally Doped $BaFe_2(As,P)_2$. *Phys. Rev. Lett.* **121**, 027001 (2018).

[27] M.-C. Lee, I. Kwak, Y. Lee, B. Lee, B. C. Park, T. Wolf, T. W. Noh, K. Kim. Nematic response revealed by coherent phonon oscillations in $BaFe_2As_2$. *Phys. Rev. B* **105**, 024501 (2022).

[28] D. Stricker, J. Mravlje, C. Berthod, R. Fittipaldi, A. Vecchione, A. Georges, D. van der Marel. Optical Response of Sr_2RuO_4 Reveals Universal Fermi-Liquid Scaling and Quasiparticles Beyond Landau Theory. *Phys. Rev. Lett.* **113**, 087404 (2014).

[29] M. Obergfell, J. Demsar. Tracking the Time Evolution of the Electron Distribution Function in Copper by Femtosecond Broadband Optical Spectroscopy. *Phys. Rev. Lett.* **124**, 037401 (2020).

[30] L. Perfetti, P. A. Loukakos, M. Lisowski, U. Bovensiepen, H. Eisaki, M. Wolf. Ultrafast Electron Relaxation in Superconducting $Bi_2Sr_2CaCu_2O_{8+\delta}$ by Time-Resolved Photoelectron Spectroscopy. *Phys. Rev. Lett.* **99**, 197001 (2007).

[31] A. P. Mackenzie, S.-I. Ikeda, Y. Maeno, T. Fujita, S. R. Julian, G. G. Lonzarich. The Fermi Surface Topography of Sr_2RuO_4. *J. Phys. Soc. Jpn.* **67**, 385 (1998).

[32] V. J. Emery. Theory of high-T_c superconductivity in oxides. *Phys. Rev. Lett.* **58**, 2794 (1987).

[33] K. M. Shen, N. Kikugawa, C. Bergemann, L. Balicas, F. Baumberger, W. Meevasana, N. J. C. Ingle, Y. Maeno, Z.-X. Shen, A. P. Mackenzie. Evolution of the Fermi Surface and Quasiparticle Renormalization through a van Hove Singularity in $Sr_{2-y}La_yRuO_4$. *Phys. Rev. Lett.* **99**, 187001 (2007).

[34] M. H. Fischer, E.-A. Kim. Mean-field analysis of intra-unit-cell order in the Emery model of the CuO_2 plane. *Phys. Rev. B* **84**, 144502 (2011).

[35] K. Rościszewski, A. M. Oleś. Charge-transfer model for the electronic structure of layered ruthenates. *Phys. Rev. B* **91**, 155137 (2015).

[36] N. Shirakawa, K. Murata, Y. Nishihara, S. Nishizaki, Y. Maeno, T. Fujita, J. G. Bednorz, F. Lichtenberg, N. Hamada. Novel Hall-Coefficient Behavior in Superconducting Sr_2RuO_4. *J. Phys. Soc. Jpn.* **64**, 1072 (1995).

[37] A. P. Mackenzie, N. E. Hussey, A. J. Diver, S. R. Julian, Y. Maeno, S. Nishizaki, T. Fujita. Hall effect in the two-dimensional metal Sr_2RuO_4. *Phys. Rev. B* **54**, 7425 (1996).

[38] M. Zingl, J. Mravlje, M. Aichhorn, O. Parcollet, A. Georges. Hall coefficient signals orbital differentiation in the Hund's metal Sr_2RuO_4. *npj Quantum Mater.* **4**, 35 (2019).

[39] T. Imai, A. W. Hunt, K. R. Thurber, F. C. Chou. ^{17}O NMR Evidence for Orbital Dependent Ferromagnetic Correlations in Sr_2RuO_4. *Phys. Rev. Lett.* **81**, 3006 (1998).

[40] A. Chronister, M. Zingl, A. Pustogow, Y. Luo, D. A. Sokolov, F. Jerzembeck, N. Kikugawa, C. W. Hicks, J. Mravlje, E. D. Bauer, J. D. Thompson, A. P. Mackenzie, A. Georges, S. E. Brown. Tuning the Fermi liquid crossover in Sr_2RuO_4 with uniaxial stress. *npj Quantum Mater.* **7**, 113 (2022).

[41] X. Wang, E. Berg. Scattering mechanisms and electrical transport near an Ising nematic quantum critical point.

Phys. Rev. B **99**, 235136 (2019).

[42] V. S. de Carvalho, R. M. Fernandes. Resistivity near a nematic quantum critical point: Impact of acoustic phonons. *Phys. Rev. B* **100**, 115103 (2019).

[43] L. E. Vieira, V. S. de Carvalho, H. Freire. DC resistivity near a nematic quantum critical point: Effects of weak disorder and acoustic phonons. *Ann. Phys. (NY)* **419**, 168230 (2020).

[44] C. A. Marques, L. C. Rhodes, R. Fittipaldi, V. Granata, C. M. Yim, R. Buzio, A. Gerbi, A. Vecchione, A. W. Rost, P. Wahl. Magnetic-Field Tunable Intertwined Checkerboard Charge Order and Nematicity in the Surface Layer of Sr_2RuO_4. *Adv. Mater.* **33**, 2100593 (2021).